frontiers | Frontiers in Physics

TYPE Original Research
PUBLISHED 05 December 2022
DOI 10.3389/fphy.2022.1048577

OPEN ACCESS

EDITED BY
Wenjun Liu,
Beijing University of Posts and Telecommunications (BUPT), China

REVIEWED BY
Sergey Sukhov,
Institute of Radio-Engineering and Electronics (RAS), Russia
Shuming Jiao,
Peng Cheng Laboratory, China
Mostafa Agour,
Aswan University, Egypt

*CORRESPONDENCE
Xingpeng Yan,
yanxp02@gmail.com

†These authors have contributed equally to this work and share first authorship

SPECIALTY SECTION
This article was submitted to Optics and Photonics, a section of the journal Frontiers in Physics

RECEIVED 19 September 2022
ACCEPTED 07 November 2022
PUBLISHED 05 December 2022

CITATION
Liu X, Yan X, Wang X, Jing T, Li P, Song C, Qu Q and Jiang X (2022), Generation of phase-only holograms with high-diffraction-order reconstruction by a U-Net-based neural network: A phase grating perspective.
Front. Phys. 10:1048577.
doi: 10.3389/fphy.2022.1048577

Generation of phase-only holograms with high-diffraction-order reconstruction by a U-Net-based neural network: A phase grating perspective

Xinlei Liu[1†], Xingpeng Yan[1*†], Xi Wang[1,2], Tao Jing[1], Pei Li[3], Cheng Song[1], Qiang Qu[1] and Xiaoyu Jiang[1]

[1]Department of Information Communication, Army Academy of Armored Forces, Beijing, China, [2]State Key Laboratory of Precision Measurement Technology and Instruments, Department of Precision Instruments, Tsinghua University, Beijing, China, [3]R&D Center for Intelligent Control and Advanced Manufacturing, Research Institute of Tsinghua University in Shenzhen, Shenzhen, China

Implicit periodic structure in phase-only holograms will result in many diffraction orders in the diffraction field. We analyzed the diffraction pattern from a phase gratings point of view and proved that the diffraction orders were jointly influenced by the phase factor, the single-beam diffraction factor, and the multibeam interference factor. According to the analysis, we proposed the high-diffraction-order angular spectrum method (HDO-ASM) for the numerical reconstruction of high diffraction orders. Different from the conventional methods of removing high diffraction orders, we chose to reconstruct target images in high diffraction orders with HDO-ASM and a U-Net-based neural network. Finally, the 4 K phase-only holograms with high-diffraction-order reconstruction were generated in 0.09s and had a mean reconstruction quality of 34.3 dB (PSNR) in the DIV2K valid dataset. Theoretical and experimental results demonstrated that there are few speckle noises and fringes in the reconstructed images of holograms generated by the proposed method.

KEYWORDS

computer-generated hologram, U-Net-based neural network, rectangular phase grating, diffraction order, imaging technology

Introduction

Compared with conventional display technologies, holography is regarded as a more promising visual display technology since it can reconstruct the whole light field of the object and can provide all visual information [1, 2]. The computer-generated hologram (CGH) is a combination of computer technology and traditional holography, which is widely used in three-dimensional display [3–7], virtual reality and augmented reality [8,

9], optical trapping [10, 11], interferometry [12, 13], microscopy imaging [14, 15], and other fields.

The spatial light modulator (SLM) is the most important equipment during the optical reconstruction of CGH, which is similar to the screen of a display device. The SLMs are mainly divided into phase-only SLM and amplitude-only SLM; the former only changes the phase of the incident light, and the latter only changes the amplitude of the incident light [16]. Compared with the amplitude-only holograms, the phase-only holograms only modulate the phase of the incident light instead of changing the amplitude of that; therefore, the intensity of the transmitted (reflected) light will hardly be changed. Thus, the phase-only hologram has higher diffraction efficiency, and the phase-only SLM is more widely used [17]. Thus, converting complex-amplitude information into phase-only information is a major difficulty to generate CGH. The traditional methods include the Gerchberg–Saxton (GS) algorithm [18], Wirtinger holography (WH) [19], the stochastic gradient descent (SGD) method [20], the error diffusion method [21], and the double-phase hologram (DPH) encoding the diffraction field directly [22]. In recent years, with the development of neural networks, researchers have tried to use it to generate phase-only holograms. Shi et al. used a large-scale CGH dataset as the training dataset of the deep neural networks (DNN), and the trained network model could generate photorealistic colored 3D hologram from a single RGB-depth image in real time, the reconstructed images of which were rich in detail and had a high reconstruction quality [23]. Wu et al. proposed a dense encoder–decoder network called Dense-Unet for realizing the reconstruction of a 3D particle field, which occupied less memory resources and required a shorter training time [24]. Lee et al. designed a structure of network which took multiple images of different depths as inputs and calculated the complex hologram as an output [25]. This method has generated holograms with multiple depths, but some additional problems have not been solved, such as occlusion or speckle reduction. An end-to-end convolutional neural network framework has been designed to rapidly generate holograms from the directly recorded images of real-world scenes, which contain depth cues, but the reconstruction quality still needed to be improved [26]. Wu et al. proposed an autoencoder-based neural network (holo-encoder) in an unsupervised manner, which could fast generate phase-only holograms, but the quality of the reconstructed image still needs to be improved [27].

SLMs modulate incident light through the structure similar to a matrix, which consists of a two-dimensional array of discrete pixels [28]. Because the pixelated SLM has a discrete nature, the diffraction pattern is formed by laterally and vertically shifted replicas, which are called diffraction orders [29]. Darwin et al. researched the effect of extra diffraction orders when phase-only holograms were illuminated by a single Gaussian beam and proposed that high-diffraction-order wasted light and had other unwanted side effects that limited the reconstruction quality [30]. He et al. regarded the CGH null system as an imaging system and developed an aberration model in Seidel formalism to analyze the high diffraction orders of CGH, and the experimental results showed that their method could reduce the adverse effect of high diffraction orders on reconstruction quality [31]. Moreover, there is a bright spot at the center of the diffraction pattern, which mainly originates from the low diffraction efficiency of SLMs and will interfere with the reconstructed images [32]. Darwin et al. derived a CGH-containing holographic information, which could project a corrective beam that destructively interferes with the zero-order beam, and improved the efficiency of the light pattern [33]. Damon et al. eliminated the zero-order beam with a checkerboard phase plate, which could shift the reconstructed images away from the center of a reconstructed pattern [34].

In the process of generating CGH through neural network, we found that generated holograms have many different diffraction patterns. Only at the center of these patterns, there is a similar reconstructed image but in the other locations there are different diffraction order reconstructions. We thought that the different diffraction order distributions were caused by different encoding methods of phase-only holograms and took one of them as an example to analyze from the phase gratings point of view. We have deduced the imaging formula of the diffraction orders and, respectively, analyzed the effect of the phase factor, the single-beam diffraction factor, and the multibeam interference factor on the high diffraction orders. Different from the aforementioned methods of limiting and removing high diffraction orders, we proposed a fresh idea that we reconstructed target images in the high diffraction orders. The $(0\text{th}, 1\text{st})$ and $(0\text{th}, -1\text{st})$ diffraction order were considered as the optimal choice to reconstruct target images. We proposed a method called high-diffraction-order angular spectrum method (HDO-ASM) to accurately calculate the numerical reconstruction of these two diffraction orders and designed a U-Net-based neural network model of two depths to fit the relationship between the diffraction field and phase-only holograms. After combining HDO-ASM with the U-Net-based neural network, the phase-only holograms which reconstruct target images in the $(0\text{th}, 1\text{st})$ diffraction order could be generated in 0.09s. Compared with traditional methods, target images reconstructed by the proposed method have higher display quality and definition.

Generation of phase-only holograms by a U-Net-based neural network

The U-Net-based neural network is a convolution neural network and consists of a contracting path to capture context and a symmetric expanding path that enables precise localization. In this paper, the trained U-Net is used to generate phase-only holograms with a high reconstruction quality. There are four steps in the training process: the reverse diffraction of target

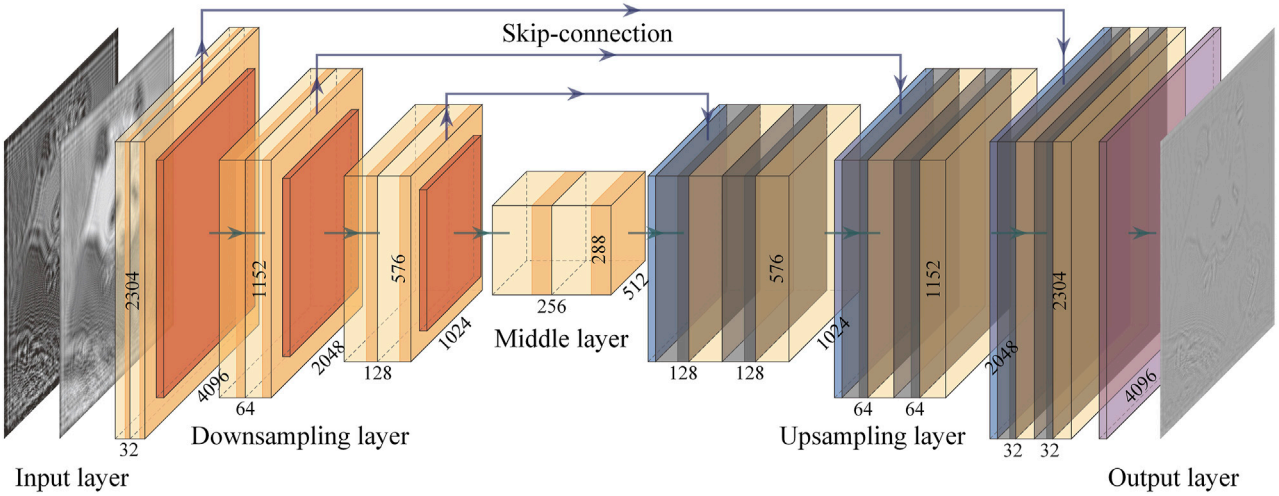

FIGURE 1
Structure of the U-Net-based neural network.

images, the generation of holograms from reverse diffraction field, the positive diffraction of holograms, and the backpropagation of errors between target images and reconstructed images.

In the first step, the distance between the imaging plane and the target image is z, and the imaging plane is parallel to the target image and has the same size. According to the angular spectrum method (ASM), the reverse diffraction field $U_z(x, y)$ in the imaging plane can be expressed as

$$U_z(x,y) = \mathcal{F}^{-1}\left\{\mathcal{F}\{U_0(x,y)\} \cdot H_z^-(f_x, f_y) \cdot L(f_x, f_y)\right\}_{f_x=\frac{x}{\lambda z}, f_y=\frac{y}{\lambda z}} \tag{1}$$

where $\mathcal{F}\{\cdot\}$ is the two-dimensional Fourier transform and $\mathcal{F}^{-1}\{\cdot\}$ is the two-dimensional inverse Fourier transform. $U_0(x, y)$ is the light field of the target image, and λ is the wavelength of the reference beam. f_x and f_y are, respectively, the spatial frequency of the diffraction field in x-axis and y-axis directions. $H_z^-(f_x, f_y)$ is the optical transfer function (OTF) in the reverse diffraction process.

$$H_z^-(f_x, f_y) = \exp\left[-jkz\sqrt{1-(\lambda f_x)^2-(\lambda f_y)^2}\right] \tag{2}$$

where $j = \sqrt{-1}$ is the imaginary unit, and $k = 2\pi/\lambda$. $L(f_x, f_y)$ is the band-limited function.

$$L(f_x, f_y) = \begin{cases} 1, |f_x| < f_{x_0} \wedge |f_y| < f_{y_0} \\ 0, \text{others} \end{cases} \tag{3}$$

where $f_{x_0} = \min\left(\frac{1}{2\beta}, \frac{M\beta}{\lambda\sqrt{z^2+M^2\beta^2}}\right)$ and $f_{y_0} = \min\left(\frac{1}{2\beta}, \frac{N\beta}{\lambda\sqrt{z^2+N^2\beta^2}}\right)$. $\wedge$ is the conjunction sign and means that both conditions should be satisfied. $M \times N$ is the resolution of target images and holograms, and β is the sampling interval, which is the same as the pixel pitch of SLM used in the follow optical experiments. When the imaging distance is very large, $L(f_x, f_y)$ can reduce the aliasing error of OTF by truncating unnecessary high-frequency signals in the input source field.

In the second step, a U-Net network model is built for generating phase-only holograms. As shown in Figure 1, the structure of the used U-Net consists of the input layer, the downsampling layers, the middle layer, the output layer, the upsampling layers, and skip-connection. The number of channels in the input layer is set to two and the number of channels in the output layer is set to one. The resolution of the input layer and output layer is set to 2,304 × 4,096. First, the amplitude of the reverse diffraction field $U_z(x, y)$ is normalized, and its real and imaginary parts are superimposed into an array. This array is input into the U-Net and the size of that is 2 × 2,304 × 4,096. In the first downsampling process, the size of input data is extended to 32 × 2,304 × 4,096 by 16 convolution operations and a ReLU function. After another convolution operation and ReLU function, the input data become the extracted feature in the highest downsampling layer. All convolution operations belong to padding-convolution and the size of the convolution kernel is 3 × 3. The extracted feature in the highest downsampling layer will be used as the input of the second downsampling layer after a max pool operation of 2 × 2, and the size of that will become 32 × 1,152 × 2048. In the second downsampling process, the size of input data is extended to 64 × 1,152 × 2048 by two convolution operations and a ReLU function. The extracted feature in the second downsampling layer can be obtained after the same operation as previously and will be used as the input of the third downsampling layer after a max pool operation. The extracted feature in the lowest downsampling layer is used as

the input of the middle layer. The extracted feature in the middle layer can be obtained after the same operation as mentioned previously, the size of which is 256 × 288 × 512. Then, the size of extracted feature in the middle layer is again changed to 128 × 576×1,024 by 128 transposed convolution operations with the convolution kernel of 2 × 2 × 2. The extracted feature will be concatenated with the extracted feature in the lowest downsampling layer through skip-connection to be used as the input of the lowest upsampling layer. In the lowest upsampling layer, the input data are changed to the extracted feature through the convolution operation and the ReLU function. The concatenation of the extracted features in the penultimate downsampling layer and the lowest upsampling layer is used as the input of the penultimate upsampling layer, and the extracted feature in the penultimate upsampling layer will be obtained in the same way. The size of the extracted feature in the highest upsampling layer is 32 × 2,304 × 4,096, and the final output data (phase-only hologram) will be obtained by a convolution operation with the convolution kernel of 32 × 1 × 1. The phase distribution of the phase-only hologram is $\phi(x, y)$, and the transmittance function is $t(x, y) = \exp[\mathrm{j} \cdot \phi(x, y)]$.

The downsampling process usually is called the encoding process, and the upsampling process usually is called the decoding process. In the encoding process, the size of the input data will decrease and the channels of that will increase. The shallow feature containing more details will be extracted. In the decoding process, the size of the input data will increase and the channels of that will decrease. The deep feature containing more semantic information will be extracted. The shallow feature and the deep feature are fused through the "skip-connection" to improve the output quality [35].

In the third step, the holograms generated in the previous step will be loaded onto the SLM. When the plane wave with unit amplitude illuminates SLM normally, the positive diffraction field of the reconstructed images in the imaging plane is expressed as

$$U(x, y) = \mathcal{F}^{-1}\left\{\mathcal{F}\{t(x, y)\} \cdot H_z^+\left(f_x, f_y\right) \cdot L\left(f_x, f_y\right)\right\}_{f_x=\frac{x}{\lambda z}, f_y=\frac{y}{\lambda z}} \tag{4}$$

where $H_z^+(f_x, f_y)$ is OTF in the positive diffraction process, which is expressed as

$$H_z^+\left(f_x, f_y\right) = \exp\left[\mathrm{j}kz\sqrt{1-(\lambda f_x)^2-\left(\lambda f_y\right)^2}\right] \tag{5}$$

In the last step, we compared the reconstructed images' amplitude $|U(x, y)|$ and the target images' amplitude $|U_0(x, y)|$ and obtained the error by the loss function L1

$$L_1 = \sum\left||U(x, y)| - |U_0(x, y)|\right| \tag{6}$$

The loss function L1 has a stable solution and does not cause the gradient exploding. The parameters of the model will be updated through the backpropagation of error. A training epoch consists of the aforementioned four steps, and the network model will generate phase-only holograms with high-quality reconstruction after lots of epochs. The maximum range of spatial frequencies is $[-1/2\beta, 1/2\beta]$ when ASM is used for numerical reproduction, and the reconstructed image is at the center of the diffraction pattern and has the same size as the hologram. Thus, there is a clear reconstructed image only at the center of the diffraction pattern but not the other parts. This leads to many different diffraction patterns of the phase-only holograms, in which the center part is similar but other parts are different. Figure 2 shows different phase-only holograms, their encoding methods, and diffraction patterns reconstructed by the S-FFT algorithm. For easy observation, the intensity of the diffraction pattern in Figure 2 has been processed. The relationship between the present intensity I' and the previous intensity I is $I' = \sqrt[4]{I}$.

We found that there is a reconstructed image in the center of all diffraction patterns, but different encoding methods result in different image distributions in other parts. In the next section, we take the diffraction pattern shown in Figure 2A as an example for detailed analysis.

Analysis and generation of phase-only holograms with high-diffraction-order reconstruction

The phase-only hologram in Figure 2A can be approximately regarded as a rectangular phase grating in the y-axis direction shown in Figure 3A. As shown in Figure 3B, the pixel pitch in the SLM is β and the length of the effective area is α. The gray area around the effective area is the dead zone, in which the incident light will not be reflected. The fill factor of the SLM is expressed as $\eta = \alpha^2/\beta^2$.

We suppose the diffraction efficiency of the SLM is γ. The pixels on a line in the SLM can be regarded a slit, and two adjacent slits are regarded as a slit combination. The resolution of SLM is the same as that of the hologram, which has M pixels in the x-axis direction and N pixels in y-axis direction. Thus, there are $N/2$ slit combinations. The transmittance function of the n − th slit combination is expressed as

$$t_n(x_0, y_0) = \left[\left(\gamma \mathrm{e}^{\mathrm{j}\phi_1} + 1 - \gamma\right)\mathrm{rect}\left(\frac{y_0 - 2n\beta + 2\beta}{\alpha}\right) + \left(\gamma \mathrm{e}^{\mathrm{j}\phi_2} + 1 - \gamma\right)\mathrm{rect}\left(\frac{y_0 - 2n\beta + \beta}{\alpha}\right)\right] \times \sum_{m=1}^{M}\mathrm{rect}\left(\frac{x_0 - m\beta + \beta}{\alpha}\right) \tag{7}$$

The spectrum of the transmittance function $t_n(x_0, y_0)$ is

$$\begin{aligned} T_n\left(f_x, f_y\right) = {} & \alpha^2 \mathrm{sinc}\left(\alpha f_x, \alpha f_y\right)\left[\gamma \mathrm{e}^{\mathrm{j}\phi_1} + \gamma \mathrm{e}^{\mathrm{j}\phi_2} \exp\left(-\mathrm{j}2\pi\beta f_y\right)\right. \\ & \left. + 1 - \gamma + (1-\gamma)\exp\left(-\mathrm{j}2\pi\beta f_y\right)\right] \times \exp\left[\mathrm{j} \cdot 4(1-n)\pi\beta f_y\right] \\ & \exp\left[\mathrm{j} \cdot (1-M)\pi\beta f_x\right]\frac{\sin\left(M\pi\beta f_x\right)}{\sin\left(\pi\beta f_x\right)} \end{aligned} \tag{8}$$

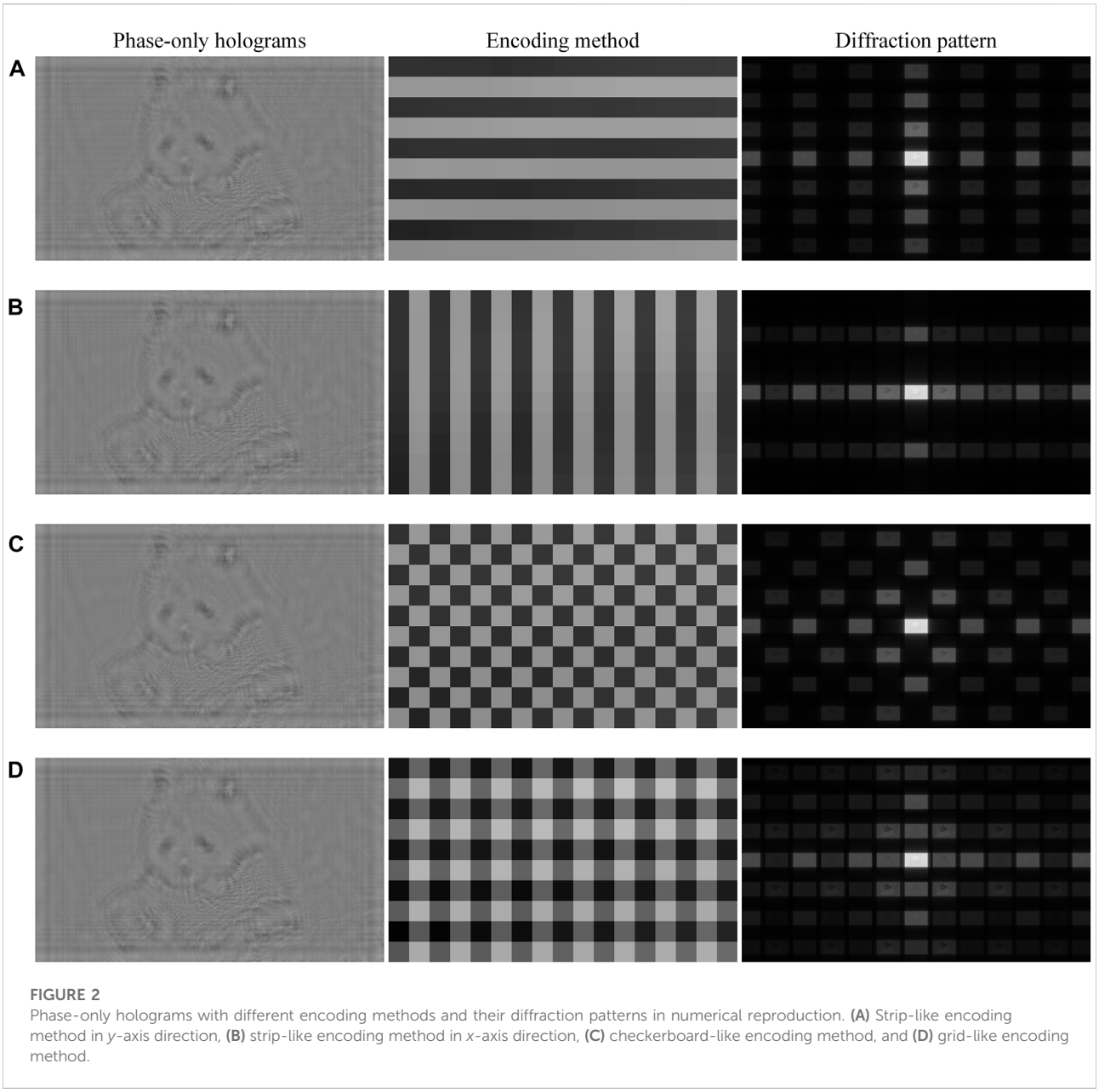

FIGURE 2
Phase-only holograms with different encoding methods and their diffraction patterns in numerical reproduction. **(A)** Strip-like encoding method in *y*-axis direction, **(B)** strip-like encoding method in *x*-axis direction, **(C)** checkerboard-like encoding method, and **(D)** grid-like encoding method.

Usually, the pixel pitch of SLM and the imaging distance are fully satisfied with Fraunhofer diffraction conditions

$$z \gg \frac{(2\alpha)^2}{\lambda} \tag{9}$$

When the plane wave with unit amplitude illuminates SLM normally, the Fraunhofer diffraction pattern generated by the n – th slit combination in the imaging plane is expressed as

$$U_n(x,y) = \frac{1}{\mathrm{j}\lambda z}\exp(\mathrm{j}kz)\exp\left[\mathrm{j}\frac{k}{2z}(x^2+y^2)\right]T_n\left(f_x,f_y\right)_{f_x=\frac{x}{\lambda z},f_y=\frac{y}{\lambda z}} \tag{10}$$

The diffraction pattern generated by the hologram is a superposition of Fraunhofer diffraction patterns generated by all slit combinations. It is expressed as

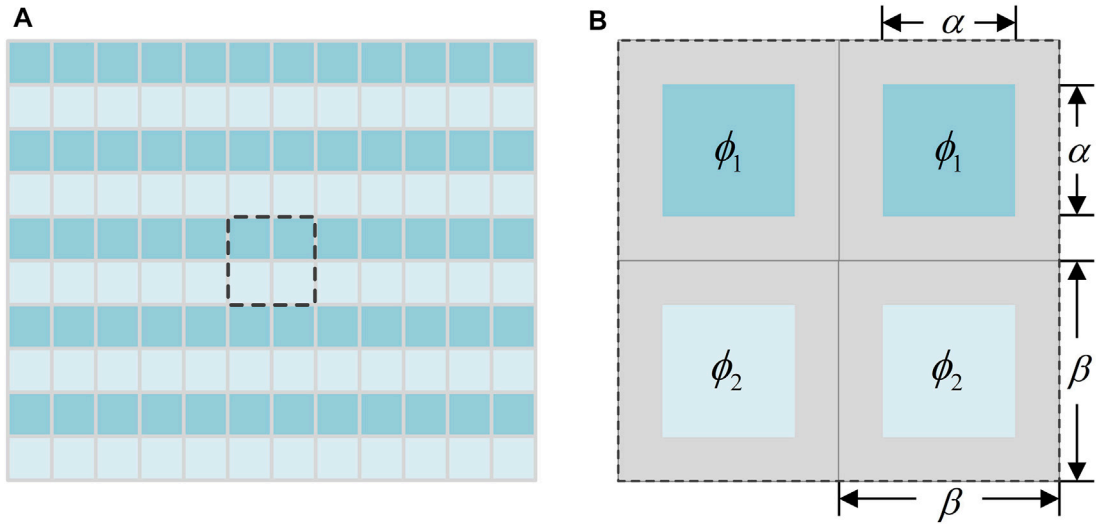

FIGURE 3
(A) SLM which has been loaded with a rectangular phase grating and **(B)** the detailed phase distribution.

$$U(x,y)=\frac{\alpha^2}{\mathrm{j}\lambda z}\exp(\mathrm{j}kz)\exp\left[\mathrm{j}\frac{k}{2z}(x^2+y^2)\right]\exp\left[\mathrm{j}\cdot(1-M)\pi\frac{\beta x}{\lambda z}\right]\exp\left[\mathrm{j}\cdot(2-N)\pi\frac{\beta y}{\lambda z}\right]\times\left[\gamma e^{\mathrm{j}\phi_1}+\gamma e^{\mathrm{j}\phi_2}\exp\left(-\mathrm{j}2\pi\frac{\beta y}{\lambda z}\right)+1-\gamma+(1-\gamma)\exp\left(-\mathrm{j}2\pi\frac{\beta y}{\lambda z}\right)\right]\times\mathrm{sinc}\left(\frac{\alpha x}{\lambda z},\frac{\alpha y}{\lambda z}\right)\frac{\sin\left(\frac{M\pi\beta x}{\lambda z}\right)\sin\left(\frac{N\pi\beta y}{\lambda z}\right)}{\sin\left(\frac{\pi\beta x}{\lambda z}\right)\sin\left(\frac{2\pi\beta y}{\lambda z}\right)} \tag{11}$$

The intensity distribution of aforementioned diffraction pattern is

$$I(x,y)=\frac{\alpha^4}{\lambda^2z^2}\left|\gamma e^{\mathrm{j}\phi_1}+\gamma e^{\mathrm{j}\phi_2}\exp\left(-\mathrm{j}\pi\frac{2\beta y}{\lambda z}\right)+1-\gamma+(1-\gamma)\exp\left(-\mathrm{j}\pi\frac{2\beta y}{\lambda z}\right)\right|^2\times\mathrm{sinc}^2\left(\frac{\alpha x}{\lambda z},\frac{\alpha y}{\lambda z}\right)\frac{\sin^2\left(\frac{M\pi\beta x}{\lambda z}\right)\sin^2\left(\frac{N\pi\beta y}{\lambda z}\right)}{\sin^2\left(\frac{\pi\beta x}{\lambda z}\right)\sin^2\left(\frac{2\pi\beta y}{\lambda z}\right)} \tag{12}$$

Equation 12 consists of the phase factor $|\gamma e^{\mathrm{j}\phi_1}+\gamma e^{\mathrm{j}\phi_2}\exp(-\mathrm{j}\pi\frac{2\beta y}{\lambda z})+1-\gamma+(1-\gamma)\exp(-\mathrm{j}\pi\frac{2\beta y}{\lambda z})|^2$, the single-beam diffraction factor $\mathrm{sinc}^2(\frac{\alpha x}{\lambda z},\frac{\alpha y}{\lambda z})$, and the multibeam interference factor $[\sin^2(\frac{M\pi\beta x}{\lambda z})\sin^2(\frac{N\pi\beta y}{\lambda z})]/[\sin^2(\frac{\pi\beta x}{\lambda z})\sin^2(\frac{2\pi\beta y}{\lambda z})]$. This indicates that the diffraction pattern of holograms is jointly influenced by the phase difference between adjacent pixels, the diffraction efficiency, the single-beam diffraction effect, and the multibeam interference effect. We will analyze each of them individually. The condition that the multibeam interference factor obtains the local maximum value in the x-axis direction is

$$M\pi\beta\frac{x}{\lambda z}=c_1\pi\wedge\pi\beta\frac{x}{\lambda z}=c_2\pi,\ c_1,c_2=0,\pm1,\pm2,\cdots \tag{13}$$

and the condition to obtain a local maximum value in the y-axis direction is

$$N\pi\beta\frac{y}{\lambda z}=d_1\pi\wedge2\pi\beta\frac{y}{\lambda z}=d_2\pi,\ d_1,d_2=0,\pm1,\pm2,\cdots \tag{14}$$

Because x and y are independent of each other in the multibeam interference factor, the local maximum value $\frac{M^2N^2}{4}$ can be obtained when

$$x=\frac{c\lambda z}{2\beta},\ c=0,\pm2,\pm4,\cdots\wedge\ y=\frac{d\lambda z}{2\beta},\ d=0,\pm1,\pm2,\cdots \tag{15}$$

These local maximum values are called the principal maximum, and corresponding bright spots are called diffraction orders. The interval between two adjacent diffraction orders is set to $\frac{\lambda z}{2\beta}$, c is the order of diffraction in x-axis direction, and d is the order of diffraction in y-axis direction. The coordinate of the center of the $(c-\mathrm{th},d-\mathrm{th})$ diffraction order is $(\frac{c\lambda z}{2\beta},\frac{d\lambda z}{2\beta})$. We found that there are only even-order diffractions in the x-axis direction, and all diffraction orders in the y-axis direction exist. Figure 4A shows the values of multibeam interference factor at different locations. For easier observation, it was set to $M,N=8$ in Figure 4A, but actually the value of M and N is usually more than 1000. In that case, the bottom radius of "cones" in Figure 4A will be very small,

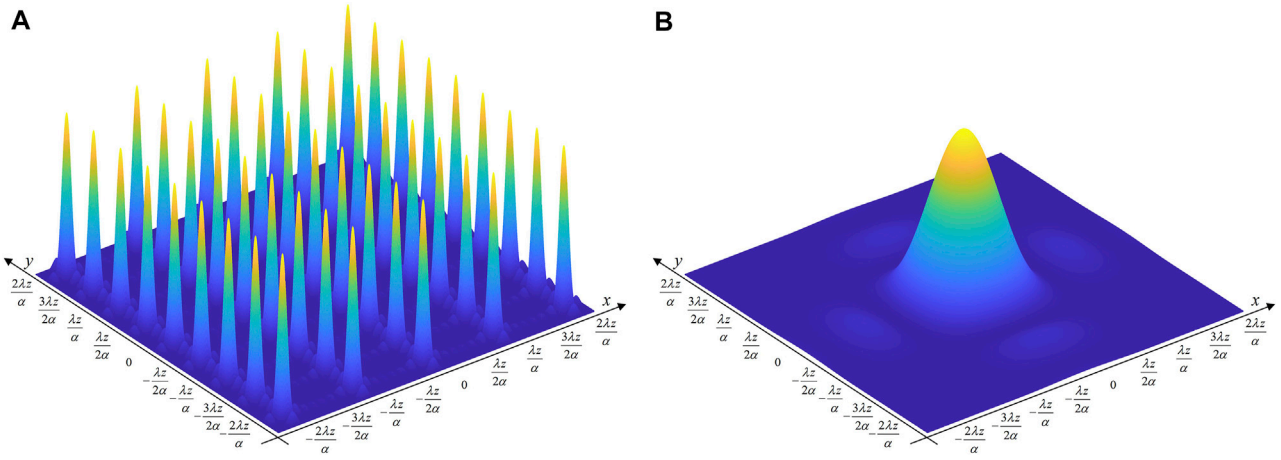

FIGURE 4
Value distribution of **(A)** the multibeam interference factor and **(B)** the single-beam diffraction factor.

the multibeam interference factor will be similar to a two-dimensional Dirac comb function, and the value of which in the location other than diffraction orders is small enough to be ignored. Thus, the next analysis for the single-beam diffraction factor and the phase factor will be around the diffraction orders in the multibeam interference factor.

The single-beam diffraction factor will achieve the minimum 0 when

$$x = \frac{p\lambda z}{2\alpha} \vee y = \frac{q\lambda z}{2\alpha},\ p, q = \pm 2, \pm 4, \pm 6, \cdots \tag{16}$$

where $\vee$ is the disjunction sign and means that at least one of the two conditions should be satisfied. When the minimum of the single-beam diffraction factor and the principal maximums in the multibeam interference factor coincide, the corresponding diffraction orders will be missing and their intensities will be modulated to 0. The missing $(c' - \text{th}, d' - \text{th})$ diffraction order satisfies the condition

$$c' = \frac{\beta}{\alpha} p \vee d' = \frac{\beta}{\alpha} q \tag{17}$$

When the fill factor η is 1, α and β are equal, and all even-order diffractions in x-axis and y-axis directions will be missing. We also found that the closer to the center of the diffraction pattern, the larger the intensity (Figure 4B).

The value of the phase factor in diffraction orders is

$$\begin{cases} 4\gamma^2 \left| \overrightarrow{OA} \right|^2, y = \dfrac{s\lambda z}{2a},\ s \text{ is odd} \\ 4\gamma^2 \left| \overrightarrow{OB} + \overrightarrow{BB'} \right|^2,\ y = \dfrac{s\lambda z}{2a},\ s \text{ is even} \end{cases} \tag{18}$$

where $\overrightarrow{OA} = \cos\left(\frac{\phi_1 - \phi_2}{2}\right) \exp\left(\text{j}\frac{\phi_1 + \phi_2}{2}\right)$, $\overrightarrow{OB} = \sin\left(\frac{\phi_1 - \phi_2}{2}\right) \exp\left(\text{j}\frac{\phi_1 + \phi_2 + \pi}{2}\right)$, $\overrightarrow{BB'} = \frac{1}{\gamma} - 1$, and $\overrightarrow{OB} + \overrightarrow{BB'} = \overrightarrow{OB'}$. $\overrightarrow{OA}$ and $\overrightarrow{OB}$ are only related to the phase ϕ_1 and ϕ_2. When s is odd, the values of the phase factor and $|\overrightarrow{OA}|^2$ are proportional. It can be found that $|\overrightarrow{OA}|^2$ and the diffraction efficiency γ are independent of each other, and the latter has the same modulation effect on all vectors. Thus, the relationship between the diffraction efficiency γ and the odd-order diffractions in y-axis direction is linear, and the former will not cause distortion of the latter in terms of intensity. When s is even, the values of the phase factor and $|\overrightarrow{OB'}|^2$ are proportional. It can be found that $|\overrightarrow{OB'}|^2$ and the diffraction efficiency γ are correlated to each other. As shown in Figure 5, $\overrightarrow{OB}$ and $\overrightarrow{BB'}$ are the two sides of the triangle, and the third side is the sum $\overrightarrow{OB'}$ of these two vectors. When the phase of $\overrightarrow{OB}$ is small, the diffraction efficiency γ will increase the value of $|\overrightarrow{OB'}|$, and when the phase of $\overrightarrow{OB}$ is large, the diffraction efficiency γ will decrease the value of $|\overrightarrow{OB'}|$. The relationship between $|\overrightarrow{BB'}|$ and the diffraction efficiency γ is negatively correlated. The lower the diffraction efficiency γ, the larger the value of $|\overrightarrow{BB'}|$ and the greater the influence on $|\overrightarrow{OB'}|$. Thus, the relationship between the diffraction efficiency γ and the even-order diffractions in y-axis direction is nonlinear, and the former will cause distortion of the latter in terms of strength. The lower the diffraction efficiency γ, the more obvious the distortion of reconstructed images.

According to the analysis of the multibeam interference factor, we marked each diffraction orders in the diffraction pattern and the location of their center in Figure 6. Also, the fill factor η and the diffraction efficiency γ was set to 81% and 60%, respectively. For easy observation, the intensity of the diffraction pattern in Figure 6 has been processed, and the processing method is the same as that of Figure 2. The previous analysis of phase factor shows that all even-order diffractions in y-axis direction are distorted in term of intensity. According to the analysis of the single-beam diffraction factor, the intensity of $(0\text{th}, 1\text{st})$ and $(0\text{th}, -1\text{st})$

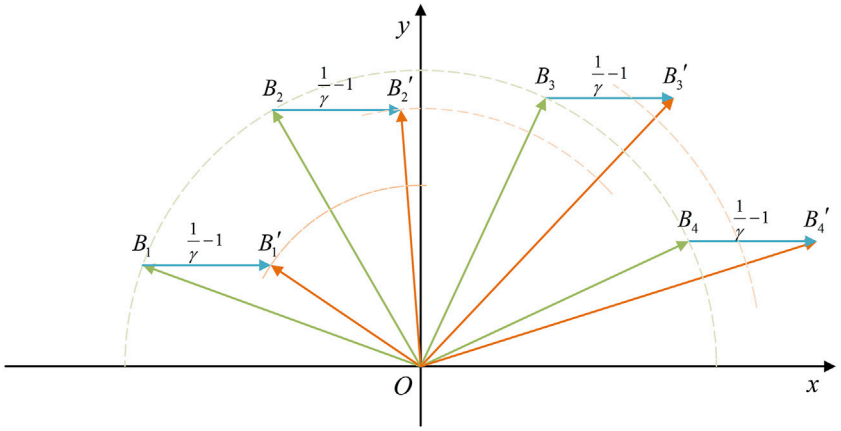

FIGURE 5
Decomposition of the phase factor when *s* is even.

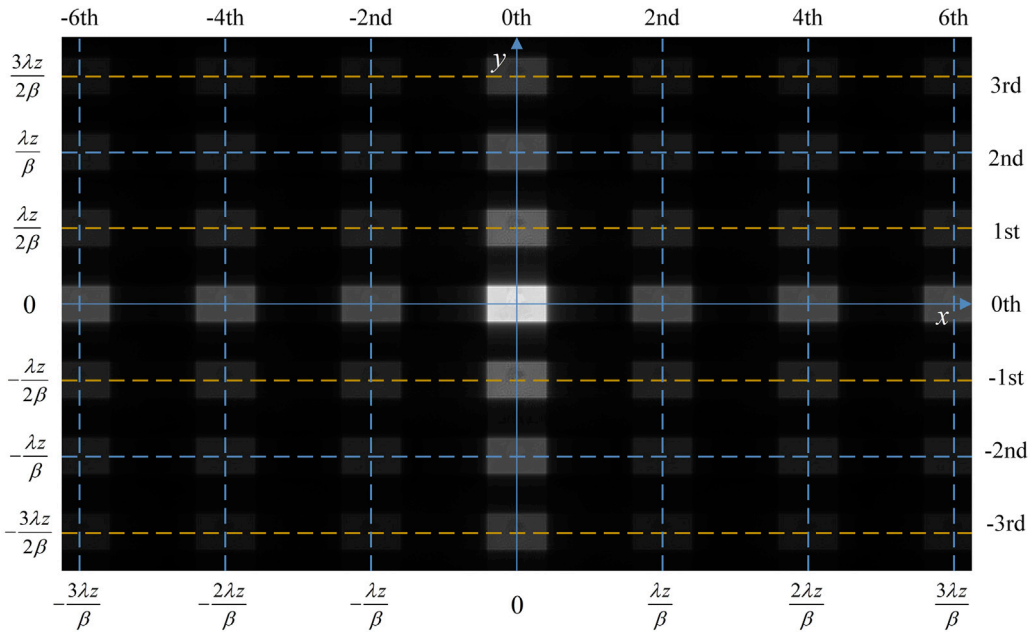

FIGURE 6
Diffraction pattern of phase-only holograms with the strip-like encoding method in *y*-axis direction.

diffraction order is largest in the odd-order diffractions in *y*-axis direction.

In the previous three factors influencing the diffraction orders, there is the phase information only in the phase factor. Thus, the reconstructed images in diffraction orders are only related to the phase factor and not the other two factors. In Eq. 18, we know that the phase factor has a same modulation on all of the odd-order diffractions; therefore, so the reconstructed images in the odd-order diffractions are the same, except for the intensity. Similarly, the reconstructed images in the even-order diffractions are also the same, except for the intensity. The diffraction patterns in Figure 2B, Figures 2C,D can also be analyzed in this way, and they will not be covered here. Because the length of our SLM in *x*-axis direction is more than that in *y*-axis direction, the larger diffraction distance is needed to filter excess diffraction orders in *x*-axis direction. However, a very large diffraction distance will increase the complexity of the optical path. Moreover, it will also lose some high frequency

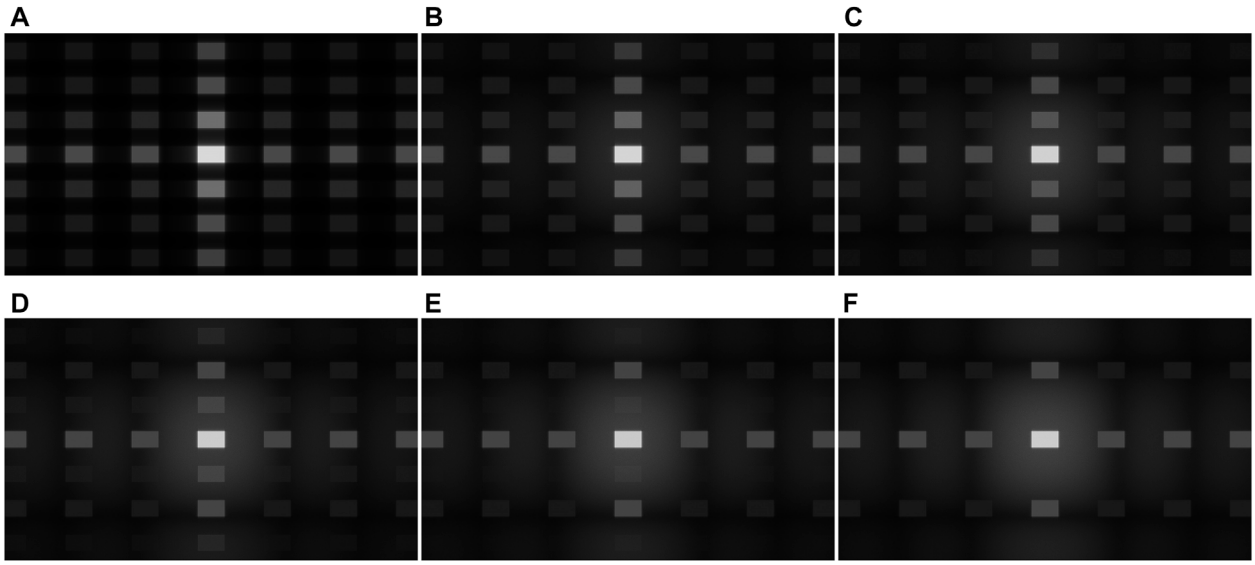

FIGURE 7
Diffraction patterns of rectangular phase gratings added with the random phase as the perturbation, the standard deviations of which are, respectively, **(A)** 0, **(B)** 0.36, **(C)** 0.73, **(D)** 1.09, **(E)** 1.45, and **(F)** 1.81.

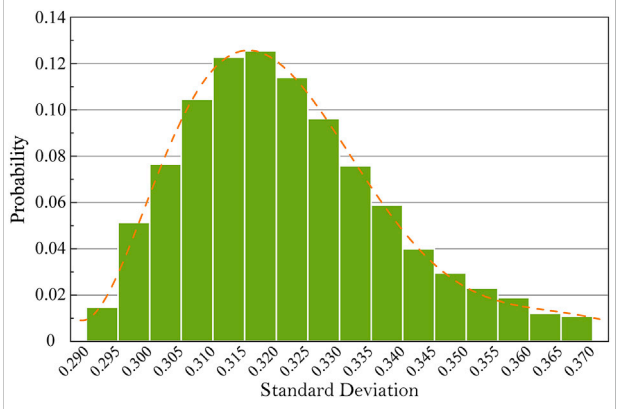

FIGURE 8
Probability of perturbations in different standard deviation ranges. The horizontal axis is the standard deviation of the random perturbation and the vertical axis is the corresponding probability.

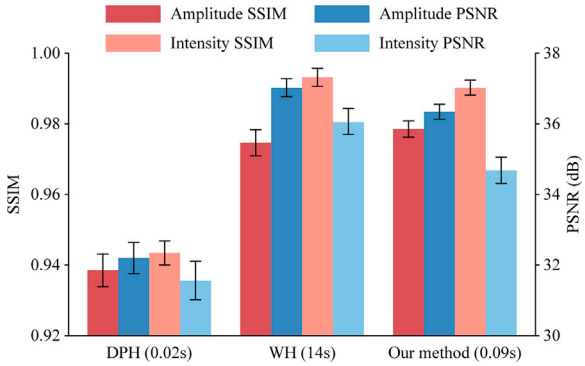

FIGURE 9
Comparison of DPH, WH, and the proposed method in reconstruction quality and speed.

information and decrease the reconstruction quality of phase-only holograms. Thus, the optimal choice to reconstruct images should be the $(0\text{th}, 1\text{st})$ or $(0\text{th}, -1\text{st})$ diffraction order instead of the $(0\text{th}, 0\text{th})$ diffraction order, which is in the center of the diffraction pattern. Finally, we decided to reconstruct target images in the $(0\text{th}, 1\text{st})$ diffraction order.

The diffraction pattern shown in Figure 6 is calculated by the S-FFT, which contains many high diffraction orders but their scales are too small to obtain errors and train the network model. Similarly, ASM is only suitable for the reconstruction of zero-th order diffraction. Here, we proposed a new method to obtain the numerical reconstruction of any high diffraction orders of phase-only holograms. In the imaging plane, the coordinate of the center of the $(c - \text{th}, d - \text{th})$ diffraction order is $(\frac{c\lambda z}{2\beta}, \frac{d\lambda z}{2\beta})$, and the vector connecting the center of the SLM to the center of the $(c - \text{th}, d - \text{th})$ diffraction order is $\vec{v} = (\frac{c\lambda z}{2\beta}, \frac{d\lambda z}{2\beta}, z)$. The direction cosines of $\vec{v}$ in x-axis and y-axis, respectively, are

$$\vec{v}_x = \frac{c\lambda z}{\sqrt{(c^2 + d^2)\lambda^2 z^2 + 4\beta^2 z^2}}, \vec{v}_y = \frac{d\lambda z}{\sqrt{(c^2 + d^2)\lambda^2 z^2 + 4\beta^2 z^2}} \tag{19}$$

FIGURE 10
Numerical reconstructed images of phase-only holograms generated by different methods. **(A)** Target images, **(B)** WH, **(C)** DPH, and **(D)** the proposed method.

The light field of reconstructed image in the $(c-\text{th}, d-\text{th})$ diffraction order is expressed exactly as

$$U'(x,y) = \mathcal{F}^{-1}\left\{\mathcal{F}\{t(x,y)\cdot \exp[jk(\vec{v}_x x + \vec{v}_x y)]\}\cdot H_z^*(f_x,f_y)\cdot L(f_x,f_y)\right\}_{f_x=\frac{x}{\lambda z}, f_y=\frac{y}{\lambda z}} \tag{20}$$

where $\exp[jk(\vec{v}_x x + \vec{v}_x y)]$ means that after the hologram is illuminated, the transmitted light (reflected light) containing phase information propagates in the direction of $\vec{v}$. This method can be applied to numerical reconstruction of all diffraction orders. When the order of diffraction is $(0\text{th}, 1\text{st})$, $\vec{v}_x$ and $\vec{v}_y$ are, respectively, $\vec{v}_x = 0$ and $\vec{v}_y = \frac{\lambda}{2\beta}$ under the paraxial approximation. We replace Eq. 20 with Eq. 4, and the rest of the method about generating phase-only holograms by U-Net remains the same. In this way, the phase-only holograms to reconstruct target images in $(0\text{th}, 1\text{st})$ order diffraction will be generated.

Experiment and discussion

The imaging distance z is set to 10 mm. In this imaging distance the relationship between complex-amplitude information and pure-phase information is not too complex; therefore, a U-Net network model with only two downsampling layers has enough fitting ability to fit the aforementioned relationship. Moreover, the lower depth means the less

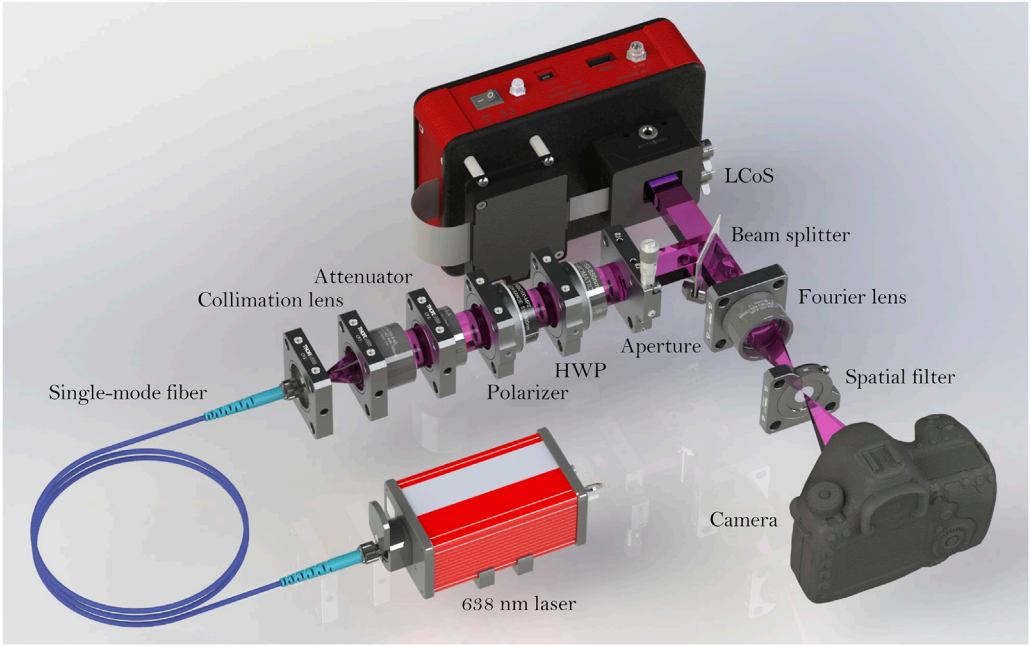

FIGURE 11
Optical experiment platform.

memory usage and computing time. The resolution of target images is 2,160 × 3,840 (4 K), and because there are obvious fringes at the edge of reconstructed images, we increase the resolution to 2,304 × 4,096 by zero-filling. The numerical platform is based on Python 3.8.13, PyTorch version 1.11.0, and CUDA version 11.6. The used U-Net neural model is trained in NVIDIA Quadro GV100 and used for generation of phase-only holograms in NVIDIA GeForce RTX 3090ti. The DIV2K-train-HR is used as the training dataset of the network model, and the Adam optimizer for optimizing the weights and biases has a learning rate of 0.0005. The model was trained 50 epochs and it cost about 3 h.

The premise of the aforementioned analysis of diffraction pattern is that phase-only holograms with the strip-like encoding method in *y*-axis direction is approximated to a rectangular phase grating. However, aforementioned holograms should actually be the combination of the rectangular phase grating and some perturbations, and it is these perturbations that bring about the reconstructed images in the diffraction orders. Moreover, perturbations also break the regularity of the phase distribution to a certain extent, which will cause changes in the distribution of high diffraction orders. In order to study this change more intuitively, we added some random phase with different standard deviations to the rectangular phase grating with a phase difference of $3\pi/5$. Figure 7 shows the diffraction patterns of the new rectangular phase gratings. We can find that as perturbations increase, the intensity of odd-order diffractions in *y*-axis direction becomes smaller and smaller, and the noises in the center of the diffraction pattern are also more and more obvious. When the standard deviation of perturbations is more than 1, it is difficult to observe the odd-order diffractions.

The Flickr2K dataset was input into the trained network model, and 2,650 phase-only holograms were generated. Each hologram can be regarded as a combination of a rectangular phase grating and the perturbation. We calculated the standard deviation of perturbations and counted the probability of perturbations which was distributed in different standard deviation ranges. The result is shown in Figure 8. It can be found that the standard deviation of perturbations is less than 0.36 in the vast majority of phase-only holograms, which means that the odd-order diffractions of holograms generated by the proposed method are more obvious than that in Figure 7B. Thus, it can be considered that holograms generated by the proposed method have clear diffraction patterns.

We have used DIV2K valid dataset to test the reconstruction quality and computing time of DPH, WH, and the proposed method. The results are shown in Figure 9. The holograms with 34.3 dB (intensity PSNR) have been generated by the proposed method in 0.09s. It can be found that the proposed method has a more excellent and balanced performance in quality and speed compared with the other traditional methods.

In the paper, the imaging distance is set to 10 mm in both numerical and optical experiments. We have also tested the

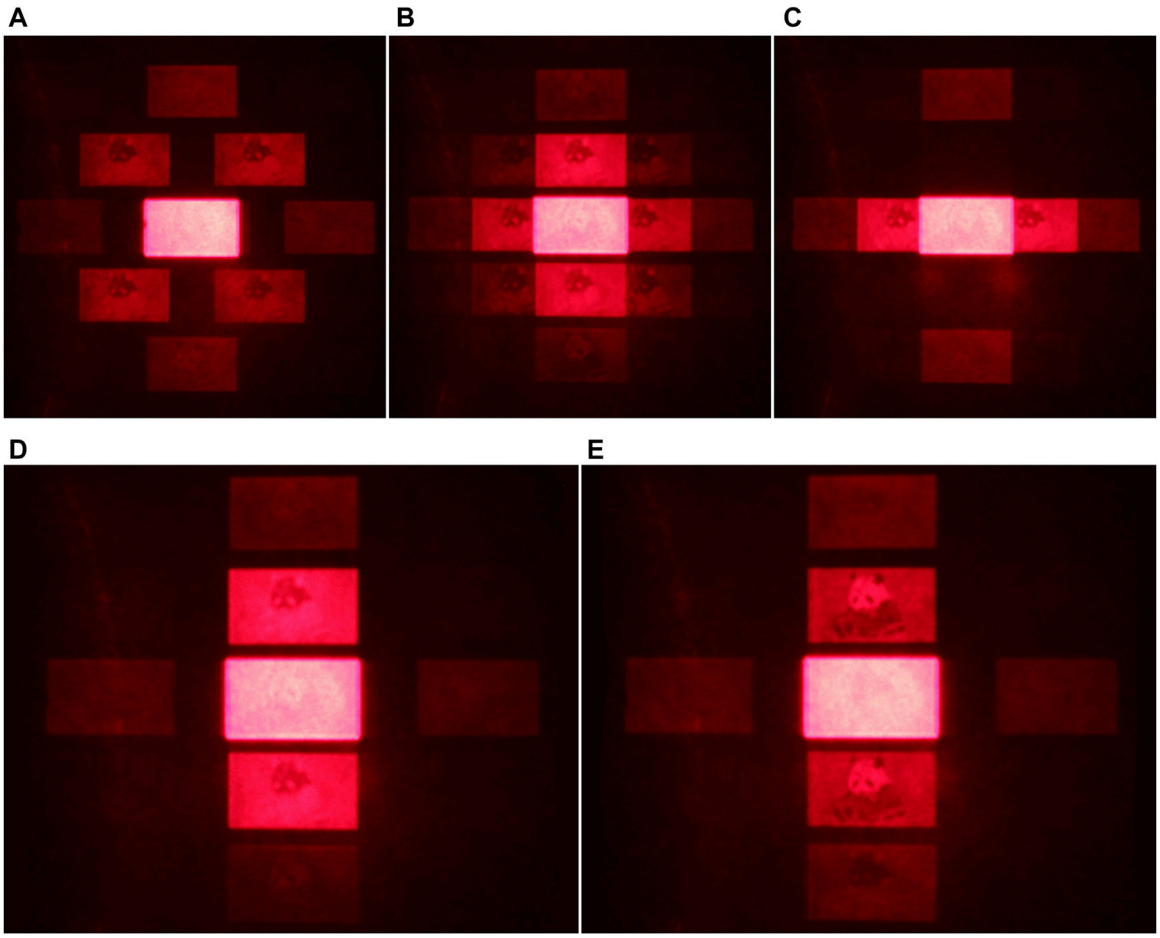

FIGURE 12
Optical diffraction patterns of phase-only holograms with different encoding methods. **(A)** Checkerboard-like encoding method, **(B)** grid-like encoding method, **(C)** strip-like encoding method in *x*-axis direction, **(D)** strip-like encoding method in *y*-axis direction, and **(E)** the proposed method. The diffraction distance is 120 mm, and the physical size of the reconstruction is 8.08 mm × 14.36 mm.

performance of the U-Net-based neural network using HDO-ASM in different imaging distances. The reconstruction qualities (intensity PSNR) of the proposed scheme in 30, 50, 70, and 90 mm are, respectively, 33.6, 32.7, 31.5, and 30.1 dB. It can be found that the reconstruction quality will decrease when the imaging distance increases. We think that there are two reasons for this problem. First, some high-frequency information is inevitably lost in the propagation of the diffraction field, which will be more obvious when the imaging distance increases. Second, the relationship between the diffraction field and the phase-only hologram will be more complex when the imaging distance increases; therefore, the fitting effect for that will decrease using the same network model. Thus, more downsampling layers and upsampling layers should be set when the imaging distance increases.

The difference between the conventional ASM and the proposed HDO-ASM is that the former reconstructs the target image in the zeroth diffraction order and the latter reconstructs the target image in (0th, 1st) diffraction order. There is little difference in numerical reconstruction performance between these two methods. However, according to the aforementioned analysis, the low diffraction efficiency of SLM will cause the distortion of the zeroth diffraction order in optical experiments. Thus, the advantage of the proposed method is mainly shown in optical reconstruction, which has a higher optical reconstruction quality. More details will be discussed in the optical experiments. The numerical reconstructions of different phase-only holograms are shown in Figure 10.

Figure 11 shows the configuration of the optical experiment platform. We used a nonpolarizing semiconductor laser with the wavelength of 638 (±8) nm as the reconstruction light source, which is connected to a single-mode fiber with core diameter of 4 μm. The laser emitted from the fiber end can be regarded as a point source due to the small core diameter of the fiber. The

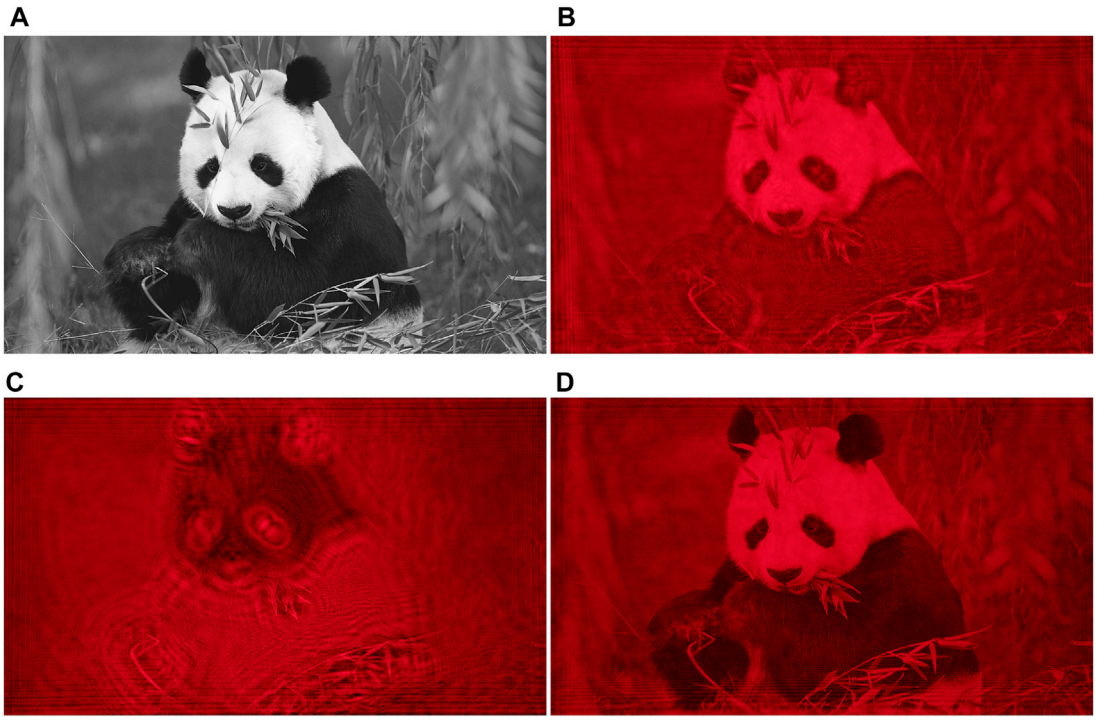

FIGURE 13
(A) Target image, **(B)** the (0th, 2nd) and **(C)** the (0th, 1st) diffraction order reconstruction of phase-only holograms with the strip-like encoding method in *y*-axis, and **(D)** the (0th, 1st) diffraction order reconstruction generated by the proposed method. The physical size of the reconstruction is 8.08 mm × 14.36 mm.

output end of the fiber was positioned at the focal point of collimated lens with the focal length of 100 mm to obtain the plane wave. We inserted a neutral density filter as an attenuator to adjust the light intensity and used a polarizer to obtain a linearly polarized light. Then, a half-wave-plate (HWP) was used to change the polarization of the light to match the optimal polarization direction of the LCoS. We positioned a rectangular aperture after the half-wave-plate to decrease the size of plane wave and obtain a rectangular profile. A 50%/50% nonpolarization beam splitter was used to split the laser. The phase-only hologram is loaded onto the nematic twisted liquid crystal LCoS with the resolution 4,094 × 2,400, whose pixel interval is 3.74 μm. The incident laser was modulated and reflected by the LCoS and propagated through the beam splitter again. We used a Fourier Lens with the focal length of 100 mm to enlarge reconstructed image and a spatial filter to allow the diffraction order we need pass through and block the other diffraction orders. A Canon EOS 5D Mark III camera equipped with an EF 100-mm f/2.8 macro lens was used to capture the magnified reconstructed image.

Figure 12 shows diffraction patterns of phase-only holograms in optical reconstruction, which correspond to the numerical reconstruction in Figure 2. The diffraction patterns shown in Figures 12A–D are generated by the U-Net-based neural network using conventional ASM, and the diffraction pattern shown in Figure 12E is generated by the U-Net-based neural network using proposed HDO-ASM. It can be found that the phase-only holograms generated by the proposed method have the same diffraction pattern. All pictures have same ISO and exposure time. It can be found that there are different high diffraction orders in the diffraction field due to different encoding methods, the intensities of which are also different. The distance between the SLM and the receiving screen is 130 mm. As shown in Figures 12B,C, at this distance the diffraction orders in *y*-axis direction can be separated, but that in *x*-axis direction cannot be separated. Only when the diffraction distance is more than 180 mm, we can observe the independent diffraction orders in *x*-axis direction. However, a very large diffraction distance will increase the complexity of the optical path and decrease the definition of the reconstructed images. Though the diffraction orders in Figure 12A can also be separated, the intensity is slightly low. Thus, the (0th, 1st) diffraction order above zeroth diffraction order and the (0th, −1st) diffraction order below that are the optimal choices to reconstruct target images. This is consistent with our previously mentioned inference.

Figure 12D shows the diffraction pattern of the phase-only hologram with the strip-like encoding method in *y*-axis direction,

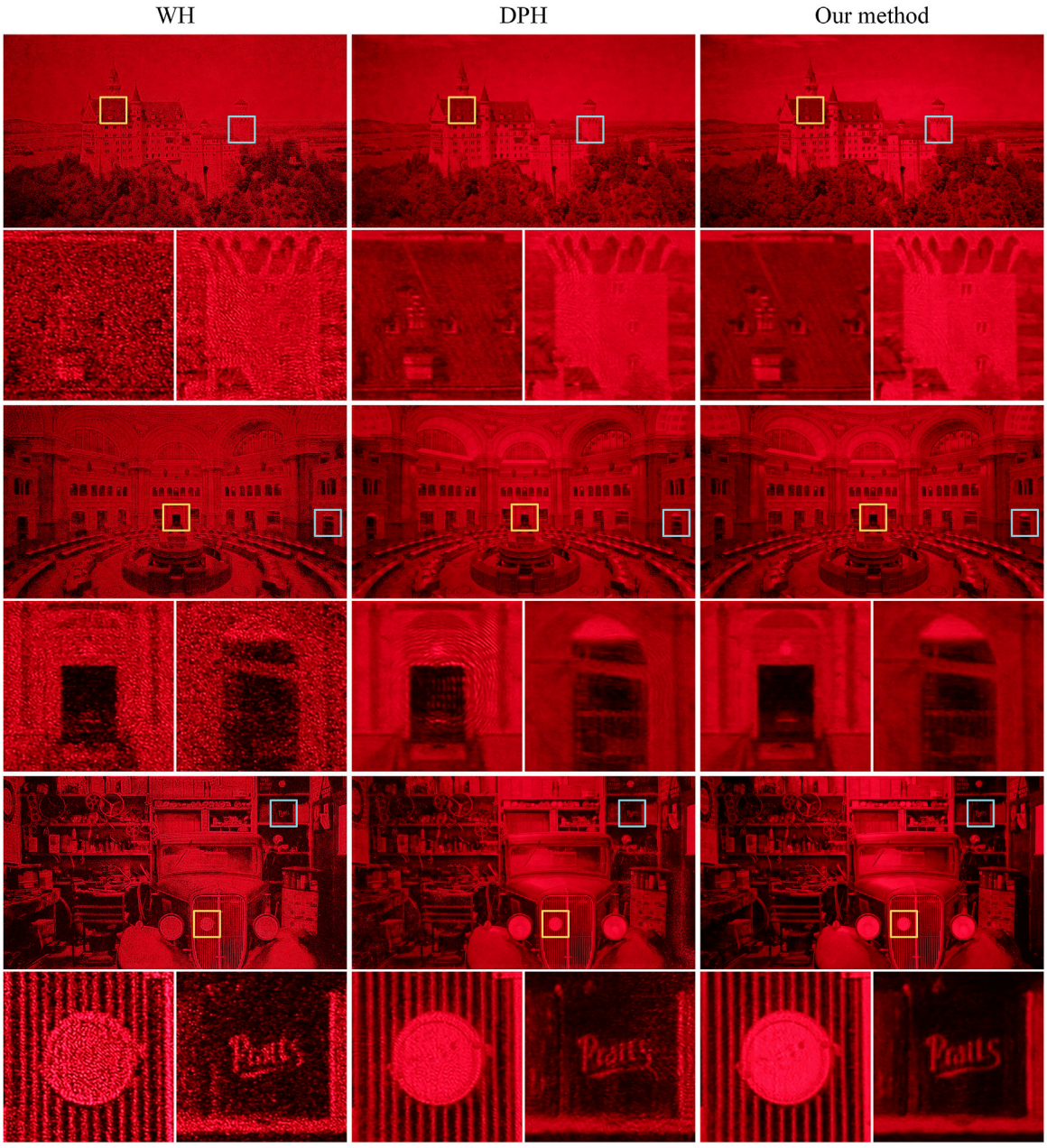

FIGURE 14
Optical reconstructed images of phase-only holograms generated by different methods. The physical size of the reconstruction is 8.08 mm × 14.36 mm.

which is generated by the U-Net-base neural network using conventional ASM and analyzed in detail in this work. Because the intensity of its zeroth diffraction order is very large, we choose to record (0th, 2nd) diffraction order (Figure 13B), which has proved to be the same as the zeroth diffraction order, except for the intensity. It can be found that the (0th, 2nd) diffraction order reconstruction is obviously distorted compared with the target image. Figure 13C shows the (0th, 1st) diffraction order above the zeroth diffraction order of holograms generated by conventional methods.

The diffraction pattern of the phase-only hologram generated by the proposed method is shown in Figure 12E, and the (0th, 1st) diffraction order of which is shown in Figure 13D. Compared with the U-Net-based neural network using ASM, the target images reconstructed in the (0th, 1st) diffraction order by the U-Net-based neural network using

HDO-ASM is not distorted and has a higher display quality. Moreover, the reconstructed images generated by the proposed method will have a higher intensity than that generated by other previously mentioned methods.

The optical reconstruction corresponding to the numerical reconstruction in Figure 10 is shown in Figure 14. The reconstructed images of WH and DPH are recorded after being separated from the DC component by a blazed grating, and the proposed method can directly record the reconstructed images in the (0th, 1st) diffraction order without the help of the blazed grating. It can be found that the optical reconstruction quality of WH decreases greatly compared with its numerical reconstruction, it is because of the aperiodic phase distribution in WH. As shown in Figure 7, when there is no periodic distribution or the periodic distribution is not obvious in the phase-only holograms, the high diffraction orders will disappear and a lot of speckle noise will fill the diffraction field. We can find that lots of speckle noises appear in the reconstructed images of WH, which causes a large reduction of the imaging quality. There are many circular fringes in the area with a low intensity in the reconstruction of DPH, which can also be observed in the numerical reconstruction. Compared with these two traditional encoding methods, there are few speckle noises and fringes in the reconstruction of phase-only holograms generated by the proposed method. In addition, it has a high definition and a similar imaging quality with the numerical reconstruction.

Conclusion

In this paper, we analyzed the diffraction pattern of phase-only holograms and found the optimal diffraction order to reconstruct target images. We proposed HDO-ASM to calculate the numerical reconstruction of any diffraction order, which was combined with a U-Net-based neural network to generate the holograms reconstructing in the optimal diffraction order. The numerical and optical result demonstrated that phase-only holograms generated by the proposed method had a better imaging quality and a higher definition compared with traditional methods.

Data availability statement

The original contributions presented in the study are included in the article/supplementary material, further inquiries can be directed to the corresponding author.

Author contributions

Conceptualization, XL and XY; methodology, XL and XY; validation, XL, XW, and TJ; formal analysis, XL, XY, and PL; data curation, XL, XW, and CS; writing—original draft preparation, XL; writing—review and editing, XL and XY; visualization, PL and QQ; supervision, XJ and XY; project administration, XY; and funding acquisition, XY. All authors have read and agreed to the published version of the manuscript.

Funding

This work was supported by the National Key Research and Development Program of China (2017YFB1104500) and the National Natural Science Foundation of China (61775240).

Conflict of interest

The authors declare that the research was conducted in the absence of any commercial or financial relationships that could be construed as a potential conflict of interest.

Publisher's note

All claims expressed in this article are solely those of the authors and do not necessarily represent those of their affiliated organizations, or those of the publisher, the editors, and the reviewers. Any product that may be evaluated in this article, or claim that may be made by its manufacturer, is not guaranteed or endorsed by the publisher.

References

1. Yaras F, Kang H, Onural L. State of the art in holographic displays: A survey. *J Display Technol* (2010) 6(10):443–54. doi:10.1109/jdt.2010.2045734

2. Hong J, Kim Y, Choi H-j, Hahn J, Park J-H, Kim H, et al. Three-dimensional display technologies of recent interest: Principles, status, and issues [invited]. *Appl Opt* (2011) 50(34):H87–115. doi:10.1364/ao.50.000h87

3. Wang D, Liu C, Shen C, Xing Y, Wang Q. Holographic capture and projection system of real object based on tunable zoom lens. *PhotoniX* (2020) 1(1):6. doi:10.1186/s43074-020-0004-3

4. Lin S, Wang D, Wang Q, Kim E-S. Full-color holographic 3D display system using off-axis color-multiplexed-hologram on single SLM. *Opt Lasers Eng* (2020) 126:105895–905. doi:10.1016/j.optlaseng.2019.105895

5. Pi D, Liu J, Wang Y. Review of computer-generated hologram algorithms for color dynamic holographic three-dimensional display. *Light Sci Appl* (2022) 11(1):231. doi:10.1038/s41377-022-00916-3

6. Li Y, Li N, Wang D, Chu F, Lee S-D, Zheng Y, et al. Tunable liquid crystal grating based holographic 3D display system with wide viewing angle and large size. *Light Sci Appl* (2022) 11(1):188–97. doi:10.1038/s41377-022-00880-y

7. Feng S, Zuo C, Yin W, Gu G, Chen Q. Micro deep learning profilometry for high-speed 3D surface imaging. *Opt Lasers Eng* (2019) 121:416–27. doi:10.1016/j.optlaseng.2019.04.020

8. He Z, Sui X, Jin G, Cao L. Progress in virtual reality and augmented reality based on holographic display. *Appl Opt* (2019) 58(5):A74–A81. doi:10.1364/ao.58.000a74

9. Chang C, Bang K, Wetzstein G, Lee B, Gao L. Toward the next-generation VR/AR optics: A review of holographic near-eye displays from a human-centric perspective. *Optica* (2020) 7(11):1563–78. doi:10.1364/optica.406004

10. Chen H, Guo Y, Chen Z, Hao J, Xu J, Wang H, et al. Holographic optical tweezers obtained by using the three-dimensional Gerchberg–Saxton algorithm. *J Opt* (2013) 15(3):035401–8. doi:10.1088/2040-8978/15/3/035401

11. Abacousnac J, Grier D. Dexterous holographic trapping of dark-seeking particles with Zernike holograms. *Opt Express* (2022) 30(13):23568–78. doi:10.1364/oe.458544

12. Dong J, Jiang C, Jia S. Digital holographic metrology based on multi-angle interferometry. *Opt Lett* (2016) 41(18):4301–4. doi:10.1364/ol.41.004301

13. Paturzo M, Pagliarulo V, Bianco V, Memmolo P, Miccio L, Merola F, et al. Digital Holography, a metrological tool for quantitative analysis: Trends and future applications. *Opt Lasers Eng* (2018) 104:32–47. doi:10.1016/j.optlaseng.2017.11.013

14. Zhang J, Sun J, Chen Q, Zuo C. Resolution analysis in a lens-free on-chip digital holographic microscope. *IEEE Trans Comput Imaging* (2020) 6:697–710. doi:10.1109/tci.2020.2964247

15. Wang H, Göröcs Z, Luo W, Zhang Y, Rivenson Y, Bentolila L, et al. Computational out-of-focus imaging increases the space–bandwidth product in lens-based coherent microscopy. *Optica* (2016) 3(12):1422–9. doi:10.1364/optica.3.001422

16. Bitou Y. Digital phase-shifting interferometer with an electrically addressed liquid-crystal spatial light modulator. *Opt Lett* (2003) 28(17):1576–8. doi:10.1364/ol.28.001576

17. Collings N, Christmas JL, Masiyano D, Crossland WA. Real-time phase-only spatial light modulators for 2D holographic display. *J Display Technol* (2015) 11(3):278–84. doi:10.1109/jdt.2014.2384913

18. Gerchberg RW, Saxton WO. A practical algorithm for the determination of phase from image and diffraction plane pictures. *Optik* (1972) 35(2):237–50.

19. Bian L, Suo J, Zheng G, Guo K, Chen F, Dai Q. Fourier ptychographic reconstruction using Wirtinger flow optimization. *Opt Express* (2015) 23(4):4856–66. doi:10.1364/oe.23.004856

20. Chen C, Lee B, Li N, Chae M, Wang D, Wang Q, et al. Multi-depth hologram generation using stochastic gradient descent algorithm with complex loss function. *Opt Express* (2021) 29(10):15089–103. doi:10.1364/oe.425077

21. Jiao S, Zhang D, Zhang C, Gao Y, Lei T, Yuan X. Complex-amplitude holographic projection with a digital micromirror device (DMD) and error diffusion algorithm. *IEEE J Sel Top Quan Electron* (2020) 26(5):1–8. doi:10.1109/jstqe.2020.2996657

22. Arrizón V, Sánchez-De-la-Llave D. Double-phase holograms implemented with phase-only spatial light modulators: Performance evaluation and improvement. *Appl Opt* (2002) 41(17):3436–47. doi:10.1364/ao.41.003436

23. Shi L, Li B, Kim C, Kellnhofer P, Matusik W. Towards real-time photorealistic 3D holography with deep neural networks. *Nature* (2021) 591(7849):234–9. doi:10.1038/s41586-020-03152-0

24. Wu Y, Wu J, Jin S, Cao L, Jin G. Dense-U-net: Dense encoder–decoder network for holographic imaging of 3D particle fields. *Opt Commun* (2021) 493:126970–9. doi:10.1016/j.optcom.2021.126970

25. Lee J, Jeong J, Cho J, Yoo D, Lee B, Lee B. Deep neural network for multi-depth hologram generation and its training strategy. *Opt Express* (2020) 28(18):27137–54. doi:10.1364/oe.402317

26. Chang C, Wang D, Zhu D, Li J, Xia J, Zhang X. Deep-learning-based computer-generated hologram from a stereo image pair. *Opt Lett* (2022) 47(6):1482–5. doi:10.1364/ol.453580

27. Wu J, Liu K, Sui X, Cao L. High-speed computer-generated holography using an autoencoder-based deep neural network. *Opt Lett* (2021) 46(12):2908–11. doi:10.1364/ol.425485

28. Wang M, Zong L, Mao L, Márquez A, Ye Y, Zhao H, et al. LCoS SLM study and its application in wavelength selective switch. *Photonics* (2017) 4(4):22. doi:10.3390/photonics4020022

29. Agour M, Kolenovic E, Falldorf C, Cv K. Suppression of higher diffraction orders and intensity improvement of optically reconstructed holograms from a spatial light modulator. *J Opt A: Pure Appl Opt* (2009) 11(10):105405. doi:10.1088/1464-4258/11/10/105405

30. Palima D, Daria VR. Effect of spurious diffraction orders in arbitrary multifoci patterns produced via phase-only holograms. *Appl Opt* (2006) 45(26):6689–93. doi:10.1364/ao.45.006689

31. He Y, Hou X, Wu F, Ma X, Liang R. Analysis of spurious diffraction orders of computer-generated hologram in symmetric aspheric metrology. *Opt Express* (2017) 25(17):20556–72. doi:10.1364/oe.25.020556

32. Cibula MA, McIntyre DH. General algorithm to optimize the diffraction efficiency of a phase-type spatial light modulator. *Opt Lett* (2013) 38(15):2767–9. doi:10.1364/ol.38.002767

33. Palima D, Daria VR. Holographic projection of arbitrary light patterns with a suppressed zero-order beam. *Appl Opt* (2007) 46(20):4197–201. doi:10.1364/ao.46.004197

34. Wong DWK, Chen G. Redistribution of the zero order by the use of a phase checkerboard pattern in computer generated holograms. *Appl Opt* (2008) 47(4):602–10. doi:10.1364/ao.47.000602

35. Sun X, Mu X, Xu C, Pang H, Deng Q, Zhang K, et al. Dual-task convolutional neural network based on the combination of the U-Net and a diffraction propagation model for phase hologram design with suppressed speckle noise. *Opt Express* (2022) 30(2):2646–58. doi:10.1364/oe.440956